AIAA 80-0141R

Dusty Gas Influences on Transport in Turbulent Erosive Propellant Flow

Alfred C. Buckingham*
Lawrence Livermore National Laboratory, University of California, Livermore, Calif.

A theoretical-numerical model is introduced that relates the influences of particles on erosive transport in a turbulent reactive boundary layer. Specifically, this discussion concerns additive particles used to suppress wall erosion in gun propellant turbulent combustion. The turbulent-particle interactions are modeled with random particulate motion computations. These produce particulate trajectories, distributions, and momenta. The interaction model includes effects of particle size, mass, and rotation as well as two-particle hard sphere collisions. The main purpose of this work is to evaluate the effects of the particles on the energy, mass, and momentum transport in the erosive wall boundary-layer region. Neglecting thermal relaxation, the heat transfer rates are found to be substantially reduced when particles are added. The most significant reduction occurs when smaller diameter (0.2 μm) particles are introduced rather than larger diameter particles (5 μm).

Introduction

THE main emphasis here is on additive-influences on erosive transport in the chemically reactive turbulent wall boundary layer driven by gun propellant combustion. Particle distributions are determined by application of a weak statistical coupling model. This model represents the interaction between the turbulent gas phase and sparse additive particle loading encountered in the core flow region, well away from the walls.[1-3] The computed distributions subsequently are applied as initial/boundary conditions to the turbulent boundary-layer computations at the wall where the particle loading is predicted to be much more substantial than that in the core flow.

Within the last two decades, renewed attention has been placed on the effectiveness of fine-grained particulate additives on reducing gun barrel erosion. These additives are placed within the bagged propellant container, or in prepared case liners surrounding the propellant, or in some cases coated directly on the barrel surface. Hassman[4] reviewed the effectiveness of TiO_2, talcum powder (hydrated magnesium silicate), and silica ablatives in reducing erosion in large calibre cannon barrels (105-155 mm bore diameter). Picard and Trask[5] discussed the possible benefits that might be found in using finely divided talcum powder rather than the TiO_2/wax combinations that had been previously favored. Recently, Lader et al.[6] presented results of a systematic study of a promising ablative liner, a thickened wall coating of silicone impregnated grease that was apparently more effective than the TiO_2/wax liner combination. Ward and his colleagues, using in-situ instrumented firing tests, traced the influence of additives by measuring changes in the in-bore heat transfer and correlated this with erosion.[7-9] In our previous work, focus was on particle size-dependent dispersal influences predicted by direct numerical simulation.[1-3]

Fundamental questions on the basic mechanisms by which additives suppress erosion remain. Some earlier theoretical investigations were aimed at isolating and systematically analyzing specific influences such as the thermal insulation provided by a thinly deposited layer of the additive coating. This was studied by Russell[10] who modeled it as a composite, nonmoving layer, obtaining results accounting for the thermal insulation properties of the layer. However, it is suspected that there remain several other significant additive influences to be identified and evaluated. The present numerical model was developed in an attempt to identify the dominant mechanisms. A number of potentially competitive processes are included in the model so that they can be isolated and tested individually as well as collectively.

Presented as Paper 80-0141 at the AIAA Aerospace Sciences Meeting, Pasadena, Calif., Jan. 14-16, 1980; submitted May 12, 1980; revision received Oct. 28, 1980.

*Physicist, Fluid Physics, H-Division, Physics Dept. Associate Fellow AIAA.

Computational Procedure and Results

General Considerations

Considerable progress has been made in improving numerical simulations of gun barrel interior ballistics. Among these, detailed averaging techniques have been developed for computing two-phase flow, stress, temperature, and bulk thermochemistry following the quasi-one-dimensional propellant bed combustion, convection, condensed phase motions, and projectile acceleration.[11-14] Experimental firing test measurements of some bulk processes, including interior pressures, in-depth wall temperatures, and projectile motions, correlate reasonably well with the better prediction methods.[15] Use is made of these predictions and experiments to provide a data base for the evolution of the inviscid flow as initial/boundary conditions for our subsequent Navier-Stokes core flow solutions.

The problem of defining a reasonable model turbulent field remains. Data is not available from actual firing tests. Hence, it is appealing to simulate the particle dispersal associated with an available, experimentally verified turbulent flow. With this in mind, we simplify the flow situation, replacing the porous combusting propellant bed face with an experimental turbulence generator, the jet plate. Flux, temperature, and pressure histories are imposed consistent with experimental or predicted inviscid internal ballistics data that have been supplied to us.[13-15]

We have previously predicted particle mass loading (ratio of particle mass density to gas mass density) for a variety of different initial additive distributions.[1-3] The particle dynamics studied in the core flow have been in the size range of 0.1-10 μm diam. Conceptually they are introduced monodispersely. Low mass loading permits evaluation of some of our computed distribution features with the trends implied by the inertial influence scaling introduced by Marble.[18,19] Subsequent discussion includes an analysis of the effects of particulate distributions on the growth of the turbulent wall boundary layer and the associated erosive wall transport.

Turbulent Core Flow

The Reynolds-averaged Navier-Stokes solutions were obtained subject to the inviscid flow boundary functions and initial conditions mentioned earlier. The numerical integrations were produced by two different methods. One was based on the explicit MacCormack differencing scheme with the two equation model closure of Wilcox and Traci. The other used a special form of the Briley-McDonald factored implicit scheme with a Jones-Launder closure model. These solutions yield the Navier-Stokes field quantities, together with turbulence kinetic energy κ and dissipation rate ϵ.[1-3]

Mean turbulent mass conservation is modeled by combining global continuity, Eq. (1), with scalar time averaging, Eq. (2), and mass averaging, Eq. (3). In the boundary-layer region, gas phase, gas surface, and surface chemical reactions require additional species conservation and production ($\psi_\ell \neq 0$) as well as multicomponent species diffusion exchange considerations, Eq. (4). The nonsimilar, reactive, multicomponent turbulent boundary-layer method originated by Kendall and Bartlett[20] was modified for quasitransient solutions and for particle mass and entropy entrainment.

Global:

$$\frac{\partial \bar{\rho}}{\partial t} + \frac{\partial(\bar{\rho}\tilde{U}_j)}{\partial X_j} = 0, \text{ assuming } \frac{n_p m_p \langle U_p \rangle}{n_g m_g \langle U_g \rangle} \ll 1.0 \tag{1}$$

Time-averaged expanded sums:

$$\phi(t) \Rightarrow \rho, p, \tau_{ij}, q_j \quad \tilde{\phi}(t) = \phi_g(t) + \phi_p(t) - \phi_g'(t)$$

$$\bar{\phi}(t_0) \equiv \frac{1}{2\Delta t}\int_{t_0-\Delta t}^{t_0+\Delta t} \phi(t)\,dt \text{ and } \bar{\phi}'(t) \equiv 0 \tag{2}$$

Mass-averaged expanded sums:

$$\phi(t) \Rightarrow U_i, H, h, I \quad \tilde{\phi}(t) = \phi_g(t) + \phi_p(t) - \phi_g''(t)$$

$$\tilde{\phi}(t_0) \equiv \frac{\overline{\rho(t_0)\phi(t_0)}}{\bar{\rho}(t_0)} \text{ and } \overline{\rho\phi''} = 0 \text{ but } \tilde{\phi}'' = \frac{\overline{\rho'\phi''}}{\bar{\rho}} \neq 0! \tag{3}$$

Species:

$$\frac{\partial(\bar{\rho}m_\ell)}{\partial t} + \frac{\partial(\bar{\rho}\tilde{U}_J m_\ell)}{\partial X_J} - \frac{\partial}{\partial X_j}\left[\bar{\rho}D_\ell^T \frac{\partial m_\ell}{\partial X_j} - j_\ell\right] = \psi_\ell$$

$D_\ell^T = D_\ell(\text{molec}) + D_\ell(\text{turb})$;

$\psi_\ell = (\text{net production rate of } \ell \text{ specie})$ (4)

Momentum:

$$\frac{\partial(\bar{\rho}\tilde{U}_i)}{\partial t} + \frac{\partial}{\partial X_j}\left[\bar{\rho}\tilde{U}_j\tilde{U}_i + \Theta\delta_{ij}p - \Theta(\bar{\tau}_{ij} - \overline{\rho U_i'' U_j''})\right] = 0 \tag{5}$$

$$\Theta \equiv \frac{v_g}{v_g + v_p} \tag{6}$$

Energy:

$$\frac{\partial(\bar{\rho}\tilde{H} - \bar{p})}{\partial t} + \frac{\partial}{\partial X_j}\left[\bar{\rho}\tilde{U}_j\tilde{H} + \Theta\bar{q}_j + \overline{\Theta\rho U_j''h''} - \Theta\tilde{U}_i(\bar{\tau}_{ij} - \overline{\rho U_i'' U_j''})\right.$$

$$\left. - \overline{\Theta U_i''\left(\tau_{ij} - \frac{\rho U_i'' U_j''}{2}\right)}\right] - \frac{\partial}{\partial X_j}\left[\sum_\ell \left(\bar{\rho}D_\ell^T \frac{\partial m_\ell}{\partial X_j} - j_\ell\right)\tilde{h}_\ell\right.$$

$$\left. - \frac{R\bar{T}}{\rho}\sum_\ell\sum_m \frac{\alpha_m D_\ell^T}{M_\ell D_{\ell m}}\left(\frac{j_\ell}{m_\ell} - \frac{j_m}{m_m}\right)\right] = 0 \tag{7}$$

In the foregoing equations, ρ, H, p, I, m_ℓ represent continuum mass density, total enthalpy, static pressure, internal energy, and ℓth species mass, respectively, while ϕ is an arbitrary variable subjected to the averaging process. For compactness, the spatial displacement and velocity components x_i, U_i are written with vector indices ($i = 1,2,3$). The overhead bar, tilde, and prime symbols denote the specific mean averages and fluctuating components as outlined in Eqs. (2) and (3). The self diffusion of the ℓth species component, species flux, mean viscous stress tensor, and heat flux vector are represented by D_ℓ, j_ℓ, $\bar{\tau}_{ij}$, and q_j, respectively.

In addition to the Reynolds' stress term, $\rho\overline{U_i''U_j''} = R_{ij}$, Eq. (5) introduces void fraction weighting. This is defined by Eq. (6). It accounts for the volumetric exclusion effects of the dispersed phase when considered mixed with the continuous phase. This weighting goes to the appropriate continuous phase limit as the relative volume occupied by the particles becomes negligible ($V_p/V_g \to 0$). It implies, as discussed by Crowe,[21] that for sparse dispersed phase concentrations, the particles contribute only slight changes to the mixture stress tensor associated with the slight change in mixture flow volume over which the stress acts.

At this first step the coupling is considered weak with no back influence from the particles to the continuous phase. The next step requires a second calculation of the mixture equations following evaluation of the particle loading distributions. This correction adjusts the distribution of mixture mass density and the mean convective fluxes of momentum and energy.

Turbulent diffusive exchange processes other than the Reynolds' stress components (i.e., turbulent heat flux, turbulent mass diffusion) are modeled by coefficients assumed linearly proportional to the locally computed eddy viscosity coefficient e_T. For example, the averaged correlation of a fluctuating scalar variable f' is approximated by the assigned proportionality coefficient N_f^* through

$$\langle(\rho u_j)'f'\rangle = \frac{e_t}{N_f^*}\frac{\partial \tilde{f}}{\partial x_j} \tag{8}$$

where the brackets indicate the appropriate averaging (mass or time) for the enclosed fluctuating quantities. Whether we apply the Launder-Spalding differential closure relations for turbulence kinetic energy (κ) and dissipation rate (ϵ) or the corresponding pseudovorticity ($\tilde{\omega}$) in the Wilcox-Traci relations, the constitutive relationship for the Reynolds' stress (R_{ij}) is assumed to have the form

$$R_{ij} = \frac{2}{3}\langle\rho\rangle\kappa - 2\langle\rho\rangle e_T\left[\bar{S}_{ij} - \frac{1}{3}\frac{\partial \tilde{U}_k}{\partial X_k}\delta_{jk}\right] \tag{9}$$

with the eddy viscosity given in terms of the appropriate closure variables by

$$e_T \equiv c_l\langle\rho\rangle\kappa^2\epsilon^{-1} \equiv \langle\rho\rangle\langle\rho\kappa\rangle\tilde{\omega}^{-1} \tag{10}$$

and where we have also introduced $\overline{S_{ij}}$ to represent the local mean flow rate-of-strain tensor.

Figure 1 illustrates the computational grid and geometry with initial conditions and boundary conditions represented symbolically. The unsteady mean scalar and vector variables were prescribed so as to match the predetermined inviscid ballistics data on velocity/pressure and temperature time histories.

The compatibility of the internal ballistics calculations with experimental data and apparent similarity of the reduced temperature and pressure pulses is illustrated in Figs. 2 and 3 for a range of barrel sizes and axial locations. This and other supporting experimental data including both axial and radial temperature distributions from 20 mm firing test of Klingenberg[22] indicate the similarity persists for a useful

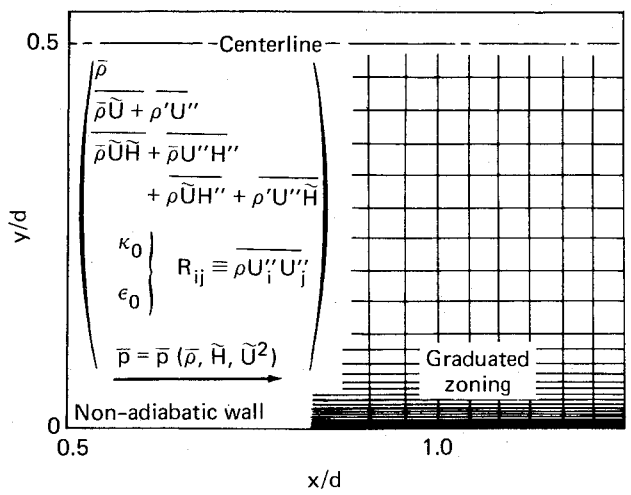

Fig. 1 Flow, computational geometry.

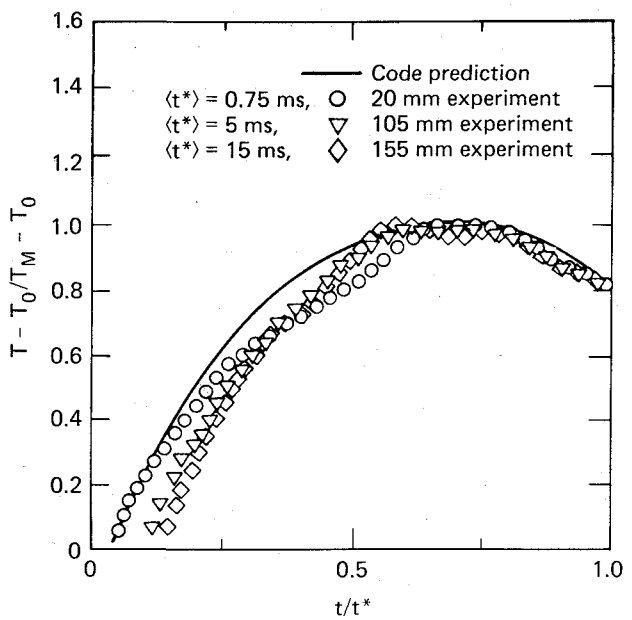

Fig. 2 Temperature-time histories of combustion products in gun barrels.

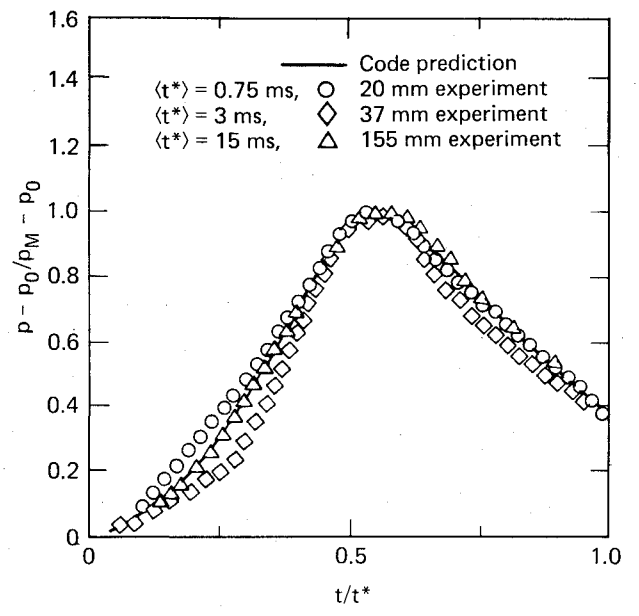

Fig. 3 Pressure-time histories of combustion products in gun barrels.

range of barrel sizes. Figure 2 is a plot of the mean core reduced temperature (subscripts 0, M, refer to initial and peak values, respectively) as a function of the dimensionless flow pulse time t/t^*. Here, t^* is the time span between measured (or calculated) onset of the significant pressure rise and the time at which the pressure pulse decays to $1/e$ of its peak value. This was chosen as a characteristic pulse normalization interval for pressure and temperature since the corresponding dimensionless pulse duration exhibits apparent independence with respect to bore size for, at least, an interesting albeit small number of interior ballistics flow situations.

The explicit values for t^* used to generate the solid curves in Figs. 2 and 3 are listed on the figures as a function of experimental barrel diameter. The cycle time was specific to an axial barrel location corresponding to the conceptual initial rest position of the projectile base. The calculated values were developed from simple wave solutions over the flow volume between the experimental measurement station (or that given by a detailed interior ballistics calculation) and the projectile base. It is emphasized, that the apparent similitude seen here is probably specific to a limited class of ballistics situations rather than evidence of a more general behavior. Certainly, similar behavior is not generally expected, even for identical bore diameters. The variation in several key ballistic parameters may be expected to produce dissimilar pulses. These include critical variations in projectile mass, propellant energy, combustion and flame spread history, and non-scaleable features relating barrel length, diameter, and in-bore projectile velocity. Nevertheless, for application to a limited number of test cases, the similarity functions are reasonably representative.

The two-dimensional viscous influences on interior ballistics flowfields are illustrated in Figs. 4 and 5. These show radial velocity profiles and temperature profiles (ratioed to peak values), respectively, at indicated dimensionless pulse times. The axial position ($x/d = 1$) for the Navier-Stokes predictions[1-3] is equivalent in the computational model to the position at which maximum erosion has been detected in large calibre cannons (i.e., the position at which the rifling begins). Qualitative agreement with experiment[22] in the development of radial profile nonuniformity is apparent for the indicated times and axial positions shown in Figs. 4 and 5.

The summary of predicted mean flow results concludes with Fig. 6, in which the calculated radial profiles of turbulence kinetic energy are plotted at the indicated pulse times and the critical axial position ($x/d = 1$). In Fig. 6 the reference turbulence kinetic energy κ_0 is the "peak" value conceptually originating at the combustion zone ahead of the propellant bed. This initial mean averaged turbulence kinetic energy, ratioed relative to the mean axial flow kinetic energy, is 0.16. Initial conditions are set compatible with the Betchov and Lorenzen[6] high intensity jet plane turbulence generator experiments for the calculations. Correlation decay with axial distance from the source is in qualitative agreement with the Uberoi and Freymuth relationships[17] that are also used to develop the autocorrelation and cross-correlation relationships used for the particle motion/turbulence coupling. This will be discussed, in more detail, subsequently.

Particle-Turbulence Coupling

Numerical simulations of ensemble averaged particle motions are used to represent the expected velocity values for the coupling between the turbulent gas and the particle cloud. From this, we obtain statistically averaged trajectories, energy partition and redistribution, and evolution of the particle spatial distribution. The statistical velocity fluctuations are obtained by applying a Monte Carlo procedure for random sampling of the turbulence velocities over a selection of independently random flow trajectories for each particle "cluster" position considered. Ensemble averages are obtained for expected values of turbulence velocities as well as the variance and standard deviation from the expected value.

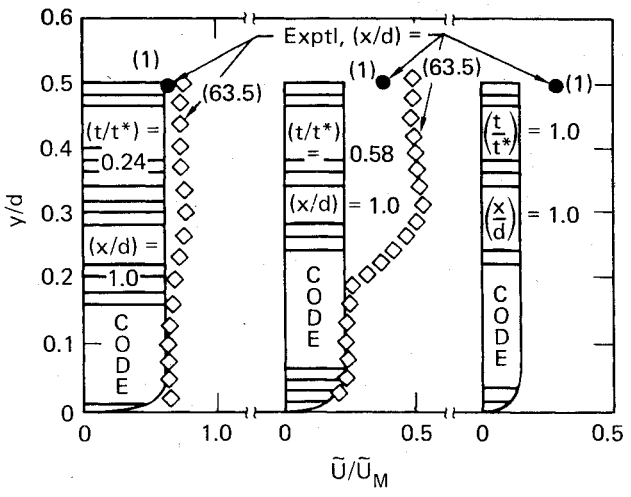

Note: change of scale

Fig. 4 Predicted mean parallel flow profiles.

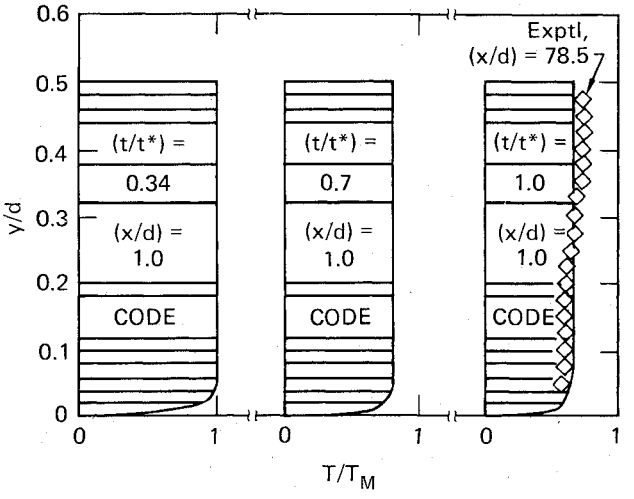

Fig. 5 Predicted mean temperature profiles.

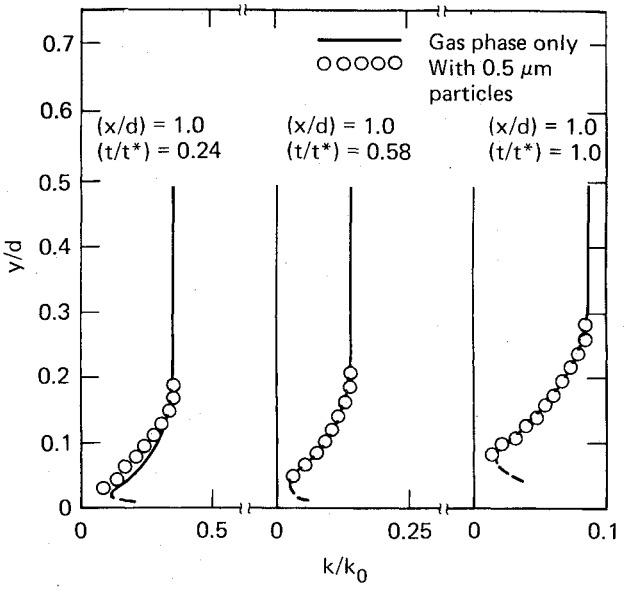

Note: change of scale

Fig. 6 Predicted turbulence energy profiles.

The expected value of the turbulence energy, summed over the phase space spectrum interval, is constrained so that it is equal to the previously computed local mean turbulence kinetic energy predicted by the Navier-Stokes solutions. An autocorrelation data base is developed from the Betchov and Lorenzen experiments[16] and Uberoi and Freymuth analysis.[17] This is used in approximating the turbulence spectrum along a phase space trajectory by applying it to form velocity recursion relations. The use of an experimental data base for the decaying turbulence spectral structure is considered necessary for at least two reasons. First, our data would otherwise be based only on computed mean averaged turbulence quantities as opposed to spectrum information. Second, our random fluctuation calculations are limited to a computationally reasonable but necessarily restricted range of wave numbers. The latter limitation is relieved by relating the spectrum form to the much broader, experimentally defined spectrum range.

Particle motions are determined by applying discrete, relative velocity dependent forces to representative particles, incrementally in time, Δt. This is necessary since all but the smallest (submicron) particles do not follow the turbulent gas phase motions directly. The particle forces derived by Crowe[21] are rewritten in a Lagrangian framework moving with the local mean gas velocity $\tilde{U}_i$. Forces considered include drag, virtual mass, Basset, Magnus, and Saffman lift, in the order indicated by Eq. (11a), to follow. Aggregate ensemble averages are used to predict representative particle group dispersion, momenta, energy, and wall collisions. Two-body hard sphere particle-particle collisions are prescribed for particle encounters. For these reasons, and other factors stated in the development, we are limited to consideration of dilute particle clouds in this study.

$$F_p = \frac{\pi d^2}{8} C_D \rho_g |u_j^* - u_{p,j}| (u_j^* - u_{p,j}) + C_l \rho_g \frac{\pi d^3}{6} \left(\frac{\partial u_j^*}{\partial t} - \frac{\partial u_{p,j}}{\partial t} \right)$$
$$+ \frac{3}{2} d^3 \sqrt{\pi \rho_g u} \int_t^{t+\Delta t} \frac{\partial}{\partial t} (u_j^* - u_{p,j}) (t-t')^{-1/2} dt'$$
$$+ \epsilon_{ijk} \frac{\pi d^2}{8} \rho_g (u_j^* - u_{p,j}) \omega_k + C_2 \sqrt{\mu \rho_g} d^2 (u_j^* - u_{p,j}) \left| \frac{\partial u_j^*}{\partial X_\perp} \right| \quad (11a)$$

In Eq. (11a), d symbolizes the particle diameter, C_D the drag coefficient, u_j^* the expected (rms) fluctuating gas velocity, $u_{p,j}$ the jth component of the instantaneous particle velocity, ω_k particle rotational velocity, and $X_\perp$ the normal direction with respect to the local particle trajectory. Following determination of the time incremental particle forces the incremental particle velocities are computed. Next, the representative particle velocity or mean motion for the particle cluster centered at a particular location (x_l, r_l) is updated by linearized Newtonian motion for constant particle mass m_p,

$$u_p(x_l, r_l, t+\Delta t) = u_p(x_l - \Delta x, r_l - \Delta r, t)$$
$$+ F_p(x_l, r_l t + \Delta t) \Delta t / m_p \quad (11b)$$

In addition to the time linearization implied by Eq. (11b) the assumption has been made that the rate of change of particle velocity is negligibly small with respect to the change in the expected value of gas fluctuation velocity u^* over a sufficiently small time increment Δt.

Axial symmetry in the governing Reynolds' averaged continuum Navier-Stokes equations [Eq. (5)] restrict the continuum data base results available for the Monte-Carlo random velocity sampling to two space dimensions, x and r, axial and radial, respectively. In the following description the brackets, $\langle\ \rangle$ designate ensemble averaging of the enclosed random variable.

The selection procedure leading to determination of the expected (rms) value of the gas fluctuations about the mean velocity,

$$u^* \equiv \sqrt{\langle u'' u'' \rangle}$$

requires that sampling of the fluctuations u'' take place on a statistically significant number of gas phase trajectories in phase space. Each trajectory represents an independently random probability density function distribution for a particle cluster centered at some fixed position and time in the computational mesh, $p(x_1, r_1, t_1)$.

Gas phase fluctuations about the mean flow speed are obtained as the weighted sum of previous increments plus a currently evaluated random fluctuation sampled from a one-component probability density function (pdf) distribution. We write the algorithm for the phase space trajectory (where the subscript j refers to the wave number),

$$u_k'' = \sum_{j=j_0}^{k-1} A_{k,j} u_j'' + \delta u_k'' \tag{12a}$$

The second term on the right-hand side of Eq. (12a) is a single point random sample. We constrain the average sum of the independent samples so that it is equal to the locally computed continuum (Navier-Stokes) value of specific turbulence kinetic energy, $(u^*)^2/2$. For N random samples in phase space, this means

$$1/(u^*)^2 \sum_{k=k_0}^{N} (\delta u_k'')^2 = 1.0 \tag{12b}$$

The process is repeated for selected additional particle clusters throughout the particle occupied regions of the computational grid.

We choose an autocovariance function from an experimental data base to broaden the range of the wave number applicability and to provide an approximation for spectrum structure information not available from our continuous phase solutions. The autocorrelation function at some time t^n is defined as a function of some "time-lagged" period, $t^n - t_0$,

$$a_{ii}(x_i, t^n - t_0) = \langle u_i''(x_i, t^n) u_i''(x_i, t_0) \rangle, i = 1,2$$

Computationally it is convenient to use the normalized, autocorrelation coefficient

$$ca_{ii}(t^n) = a_{ii}(x_i, t^n - t_0)/\langle u_i''(x_i, t_0)^2 \rangle$$

where, $ca_{ii}(t_0) \equiv 1$, at the origin, and decreases monotonically away from it.

The "history" of previous trajectory motions which enters the computation of u_k'' as seen in Eq. (12a) is weighted by functions $A_{k,j}$, that act as velocity recursion relations for computing u_k''. These are based on the experimental autocorrelations of the expanding multisource jet flow (that replaces the face of the propellant bed) in our model.[16,17] To illustrate this, Eq. (12a) is averaged, yielding

$$\langle u_k'' \rangle = \sum_{j=j_0}^{k-1} \langle A_{k,j} u_j'' \rangle + \cancelto{0}{\langle \delta u_k'' \rangle} \tag{12c}$$

This acts as a defining relation for the recursion coefficient $A_{k,j}$. Multiplying by $\langle u_m'' \rangle$, $m = m_0, m_0 + 1, \ldots K-1$, together with the autocorrelation definition, obtain

$$a_{ii}(x_i, t^k - t^m) = \sum_{j=j_0}^{k-1} A_{k,j} a_{ii}(x_i, t^m - t^{m-1}) \tag{12d}$$

which indicates the recursion relationship between the coefficient $A_{k,j}$ and the experimentally defined correlation functions.

Random velocity sampling is applied to as many as 1100 pdf trajectory paths in wave number space to obtain the data for ensemble averaging. The sampling procedure with a sufficient number of samples, incrementally approximates uniformly convergent probability integration for the set of functions f_i, of random variables x_i with probability distribution function g,

$$\int_{-\infty}^{\infty} \cdots \int_{-\infty}^{\infty} g(x_i \ldots x_p) f_i(x_i) \ldots f_p(x_p)\, dx_i \ldots dx_p \tag{13a}$$

The sampling provides the incremental statistical occurrences that are summed over a selected distribution function, replacing the integration

$$\frac{1}{N} \sum_{i=1}^{N} g(\xi^i \ldots \xi_p^i) f(\xi^i), \quad \xi_\ell^i = \chi_\ell^i w_\ell^i \tag{13b}$$

The base distribution is taken to be the Gaussian normal distribution for weighted (w_ℓ^i) phase space spectrum samples of random variable χ_ℓ^i. Selective weighting is applied using the "importance sampling" techniques developed primarily for chemical physics applications. Importance sampling is a method for systematic selective sampling of the most interactive portions of the spectrum. It accelerates convergence while reducing the required number of selections and computations.[23] Trial weighting functions are listed in Eq. (13c). Best results for the present cases were achieved using the parabolic bin weighting, $w_\ell = 2(1 - \delta^2)$, which favors the energetic low wave number portion of the spectrum,

$$\begin{aligned} w_\ell = {} & 1. \\ & 3\delta/2, \\ & 1/2\delta, \\ & 3(1-\delta), \\ & 2(1-\delta^2). \end{aligned} \qquad \delta_k \equiv \frac{\delta(k-1,k)}{\Delta}, \quad \Delta \equiv \sum_k \delta_k \tag{13c}$$

The statistical formulation that is unbounded physically is invalid at and near the walls ($r \pm \infty$). However, in the current model the core flow solutions, for which the statistical particle distributions apply in the interior, are overlapped by boundary-layer solutions strictly valid near the wall.

The contours of predicted particle mass loading distributions are shown for 0.3 and 5 μm monodisperse additive particle sizes in Figs. 7 and 8, respectively. The initial particle distributions are represented by the cross-hatched areas in the figures. Particle mass loading is identified in the subsequent plots by the density parameters

$$k^* \equiv \frac{\rho_p}{\rho_g} \text{ and } k_p \equiv \frac{\rho_p + \rho_g}{\rho_g} = 1 + k^* \tag{14}$$

The smaller particles relax with relative rapidity to the local turbulent flow motion so that their dispersal pattern almost matches that predicted by assuming instantaneous equilibration to the local gas velocities. The larger particles, however, lag the local flow currents, creating narrower dispersion patterns and shortened penetration distances.

At this stage in the modeled turbulence particle coupling, the particle populations (at least in the core flow) are treated as sufficiently sparse so as to approach the inertial "weak" viscous coupling limit theoretically examined by Marble.[18,19] In the present approach both explicitly treated particle-particle collisions and inertial feed-back influences of k^* on the transporting turbulent gas phase (by an iterative step revising the basic flow results) are included. In addition, an approximation is made to account for the changes in acoustical energy loss from the turbulent flow due both to

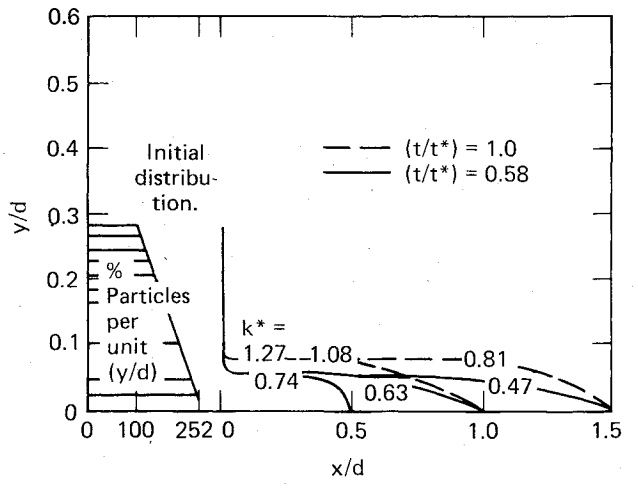

Note: change of scale

Fig. 7 Contours of 0.3 μm particle mass loading on boundary-layer velocity profiles.

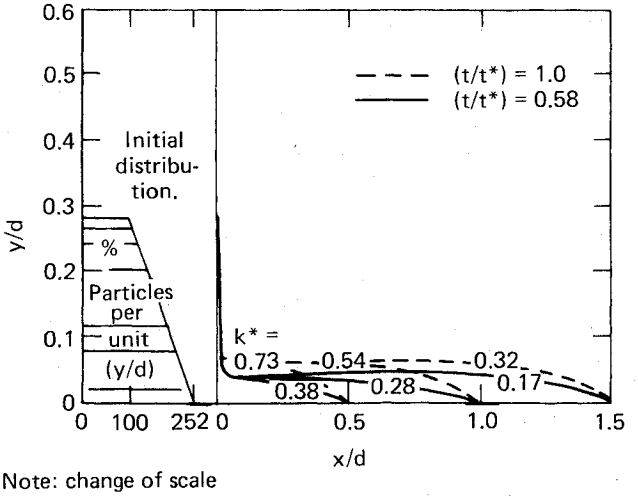

Note: change of scale

Fig. 8 Contours of 5 μm particle mass loading at designated times.

inertial damping of the turbulent oscillations and changes to the local sound speed a. The sound intensity generated by local fluctuations is represented by Lighthill's model of distributed monopole sources.[24] The source intensity is given by

$$I(r_0,t) \equiv \frac{\rho}{4\pi a}\left(\overline{\frac{\mathrm{d}}{\mathrm{d}t}\dot{V}}\right)^2 \tag{15}$$

The term in parentheses is the fluctuation averaged time derivative of the volumetric rate of change of a control volume of fluid. The fluid mixture density, $\rho=\rho_p+\rho_g$, and sound speed, $a=a(\rho,\tilde{T})$, both incorporate effects of the particle mass loading in this level of approximation.

Core Influences Matched to Wall Boundary Layer

The boundary conditions for the boundary-layer solutions together with the computed particle concentration, momenta, and energy distributions are obtained from the core flow computations. The core computations are, in fact, global. They are carried out (albeit coarsely) all the way from centerline to passive (impermeable) wall. The boundary layer region is then "magnified" by applying subsequent nonsimilar reacting, turbulent, multicomponent boundary-layer solutions to the region near the wall. The matching of the separate computational domains, each with its own distinct formulation and computational method, avoids the numerical and practical difficulties arising from the vast differences in time and length scales associated with each of the two major flow regions: turbulent core and wall boundary layer.

In previous work[1,2] additional conditions were found and specified for the "edge" matching of the core to the boundary-layer flow. The more significant features of the matching include determining the edge of the unsteady turbulent boundary layer by a conditional requirement that the turbulent kinetic energy and dissipation tend asymptotically to a finite (minimum) value at the edge interface (as opposed to vanishing altogether). The new conditions are summarized by comparing the upper level (above the dashed line) conditions for conventional boundary-layer matching with the current conditions (below the line) in Eq. (16), to follow. The left column refers to the turbulent core e. The right column to the wall boundary layer w. The central column is the overlap (matching) region. Single primes denote differentiation with respect to the local wall normal metric and the term f'' implies the normal derivative of the parallel velocity.

$$\begin{aligned} &U_e=\tilde{U}_e;\ \kappa,\epsilon,f''\to 0;\ (R_{ij})_w=F(\kappa,\epsilon,\tilde{U}_e) \\ &(R_{ij})_e\approx 0 \quad \text{as } y_w\to y_e \\ &\text{---} \\ &U_e=\tilde{U}_e+U_e'';\ \kappa',\epsilon',f''\to 0;\ (R_{ij})_w=F[\kappa,\epsilon,\tilde{U}_e,\ (R_{ij})_e] \\ &(R_{ij})_e=F(U_e'')\neq 0 \quad \text{as } y_w\to y_e \\ &\langle U_e\rangle=\tilde{U}_e \end{aligned} \tag{16}$$

Boundary Layer-Wall Transport

Additive particle concentrations are incorporated in the edge conditions through changes in the edge entropy profile, the corresponding gas state, and the altered conditions on the momentum integral due to increased mass flux. Within the boundary layer the transport exchange coefficients for multicomponent species are adjusted with "frozen" contributions from the nonequilibrium thermal and momentum relaxation for the particles.

The boundary-layer region entrains a substantial concentration of the particles in a small region of a large shear. Discounting the velocity persistence of the larger particles (for illustration purposes) the particle flow departure from that of the surrounding gas phase generally would tend to vanish (with the possible exception of the parallel component of the particle flow at the wall surface which clearly does not acquire a no-slip accommodation as do the gas molecules). At the present level of modeling, a single phase dense gas continuum replaces the mixture equations in the boundary layer. The corresponding edge mass entrainment (hence boundary-layer displacement) and entropy gradient variations (hence nonsimilar thermophysical state) are explicitly applied to develop the boundary-layer solutions.

Within the boundary-layer region, the present model predicts an outward displacement of the viscous sublayer in response to particle-induced density increase and alteration of the thermodynamic state. In addition, the molecular transport properties governing the final dissipation of energy within the viscous sublayer are altered. These changes are estimated using the Enskogg approximation (and equivalent second virial coefficient expansion) for calculating the transport coefficients.

Figures 9-11 summarize some of the predicted variations to the erosive wall transport associated with the computed additive particle loadings. Figure 9 shows the predicted variation in velocity profiles, following entrainment of 0.3 μm particles in law-of-the wall variables u^+ and y^+. Here,

$$u^+\equiv\tilde{U}/u_\sigma,\ u_\sigma\equiv\sqrt{\tau_{w/\rho}},\quad y^+\equiv yu_\sigma/\nu \tag{17}$$

and τ_w is the local wall shear. The computed variation in reduced enthalpy profiles vs boundary-layer velocity profiles for 0.3 μm particle entrainment is shown in Fig. 10. Here the

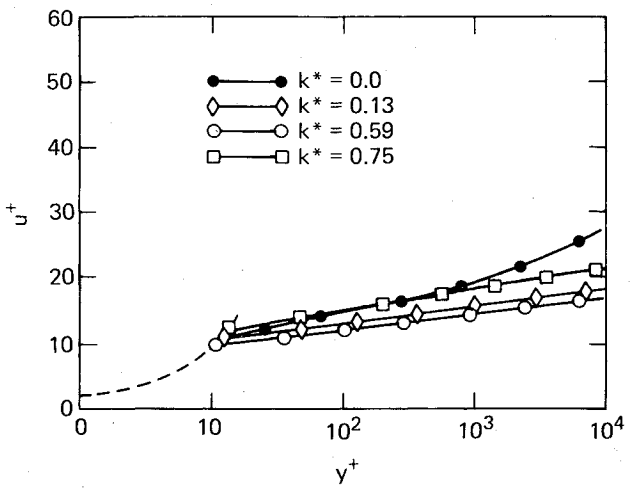

Fig. 9 Predicted effects of 0.3 μm particle loading on boundary-layer velocity profiles.

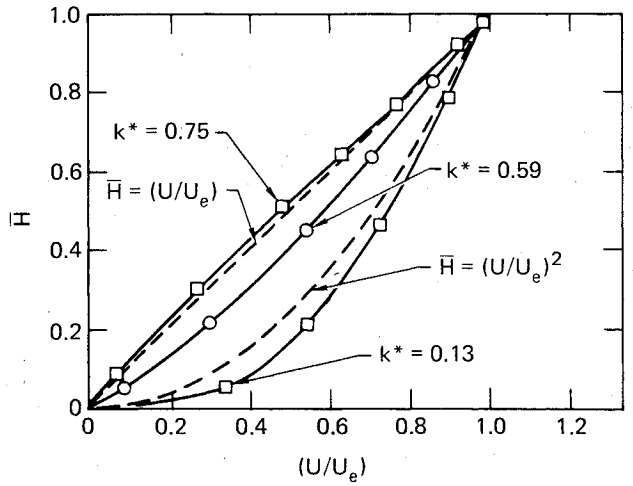

Fig. 10 Predicted effects of 0.3 μm particle loading on boundary-layer enthalpy profiles.

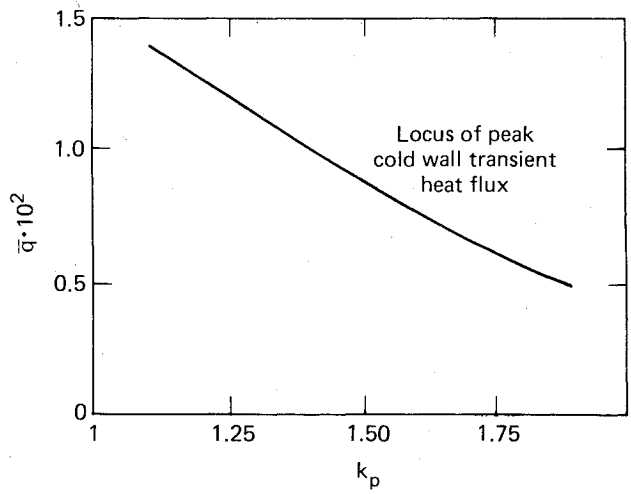

Fig. 11 Comparison of predicted effects of particle loading on cold wall heat transfer.

reduced enthalpy is given by $\bar{H} \equiv (H_0 - H_W)/(H_e - H_W)$, where H_0 is the (local) total enthalpy and H_e is the edge total enthalpy, while H_W designates conditions at a cold ($T_W = 300$ K) wall. The Reynolds' analogy (linear correlation) and quadratic dependence curves are also plotted for comparison with the computed values for designated mass loadings. In Figs. 9 and 10 the mass loading parameter k^* introduced previously is used to identify particle/boundary-layer loading levels.

Figure 11 shows the comparative reduction in dimensionless heat flux, $\bar{c}_q = \bar{q}/\bar{\rho}_e \tilde{U}_e^3$, with mass loading parameter $k = 1 + k^*$, for specified 0.3 or 5 μm additive size distributions. The current predictions indicate that significant effectiveness in reduction of the erosive heat load occurs only for the smallest additives (additive rms diameters less than 1 μm).

Summary

The emphasis here is on combining statistical and continuum flow models to assess the role of particulate additives on reducing wall erosion in turbulent propellant combustion. Current results indicate the following:

1) To be effective in erosion reduction, additives should be submicron size, preferably of the order of 0.1-0.3 μm. Larger gas-borne particles tend to move axially down the barrel with insignificant lateral dispersal even in an intense turbulence field. Hence, only the smallest size particles are entrained in the wall boundary layer in sufficient numbers to significantly reduce erosive wall heat transfer.

2) Near-wall particle concentrations provide a greater surface area to diffusion transport or chemical kinetics than the wall itself. The greater surface area directly reduces the heat transfer to the wall by intervening between the hot core combustion core region and the wall, and promotes (exothermic) gas-surface chemical reactions on the particles rather than at the wall surface.

3) Additives should be initially placed as close as possible to the wall surface. For example, particles can be wrapped around the exterior surface of bagged propellants or fixed to the interior of the casing surface of cartridge propellants. The use of particulate additives bonded to the surface rather than introduced into and convected with the combustion products may, however, be less effective. This is because the wall shear, shot-to-shot, removes the fixed particle layer. Without a renewable source of particles the wall-bonded particulate concentrations would soon be depleted during repeated firings. The gas-borne particulates, however, are reintroduced from the propellant charge at each successive firing.

4) Large populations of the smallest particles are predicted to reduce the boundary-layer shear and heat transfer primarily by displacing the boundary layer and thereby reducing the mass flux and thermal gradients.

Acknowledgments

Work performed under the auspices of the U.S. Department of Energy by Lawrence Livermore National Laboratory under Contract W-7405-Eng-48, and supported by the U.S. Army ARRADCOM Laboratories, Dover, N.J., and Aberdeen Proving Ground, Md., together with the U.S. Army Research Office (ARO), Durham, N.C. under Contract ARO 15812-MS. The writer acknowledges, with pleasure, the numerous discussions, assistance, information, and aid of the ARRADCOM Scientific Staff, particularly A. Horst, J. Lannon, I. Stobie, and J. R. Ward as well as that of the Army Research Office, particularly P. Parrish, R. Singleton, F. Schmiedeshoff, and D. Squire. The experimental data, help, and advice of G. N. Klingenberg of the Ernst Mach Institute, and theoretical discussions with S.-W. Kang, J. Levatin, and M. Ross are also acknowledged.

References

[1] Buckingham, A. C. and Kang, S.-W., "Multidimensional Interior Ballistics Computations on Wear and Erosion Mechanisms in Gun Barrels," *Proceedings of the 1979 JANNAF Propulsion Meeting*, Anaheim, Calif., March 1979, pp. 195-210.

[2] Buckingham, A. C., "Turbulent Dusty Gas Motions with Weak Statistical Coupling," AIAA Paper 79-1484, AIAA 12th Fluid and Plasma Dynamics Conference, Williamsburg, Va., July 1979.

[3] Buckingham, A. C., "Modeling Additive and Hostile Particulate Influences in Gun Combustion Turbulent Erosion," *Proceedings of the Sixteenth JANNAF Combustion Meeting*, Naval Postgraduate School, Monterey, Calif., Sept. 1979, pp. 673-690.

[4] Hassman, H., "Review and Trends of Wear Reducing Additives in Large Calibre Tank and Artillery Cannon," *Proceedings of Interservice Technical Meeting on Gun Tube Erosion and Control*, Watervliet Arsenal, Watervliet, N.Y., Feb. 1970, pp. 2.1-2-2.1-15.

[5] Picard, J. P. and Trask, R. I., "Talc, A New Additive for Reducing Gun Barrel Erosion," *Proceedings of the Tri-Service Gun Propellant Symposium 1*, Picatinny Arsenal, Dover, N.J., Oct. 1972, pp. 6.2-1-6.2-12.

[6] Lader, S., Russell, K., and Wurzel, E., "Optimization of Wear Reducing Additive for 105 mm Cartridge, Heat M456," presented at Large Calibre Weapons System Laboratory ARRADCOM, Dover, N.J., March 1979.

[7] Ward, J. R. and Brosseau, T. L., "Effect of Wear-Reducing Additives on Heat Transfer Into the 155 mm M185 Cannon," U.S. Army BRL Aberdeen, Md., Rept. BRL MR2370, Feb. 1977.

[8] Ward, J. R. and Brosseau, T. L., "Reduction of Heat Transfer to High Velocity Gun Barrels by Wear Reducing Additives," ASME Paper 77-HT-19 AIChE-ASME Heat Transfer Conference, Salt Lake City, Utah, Aug. 1977.

[9] Ward, J. R. and Freedman, E., "Assessment of the Japanese Wear-Reducing Additives," U.S. Army BRL Aberdeen, Md., Rept. ARBRL-MR-02920, May 1979.

[10] Russell, L. H., "Simplified Analysis of the Bore Surface Heat Transfer Reduction in Gun Barrels as Achieved by Using Wear-Reducing Additives," Naval Surface Weapons Center, Rept. NSWC/D1 TR-3378, Oct. 1975.

[11] Kuo, K. K., Vichnevetsky, R., and Summerfield, M., "Theory of Flame Front Propagation in Porous Propellant Charges Under Confinement," *AIAA Journal*, Vol. 11, April 1973, p. 444.

[12] Kuo, K. K., "A Summary of the JANNAF Workshop on Theoretical Modeling and Experimental Measurements of the Combustion and Fluid Flow Processes in Gun Propellant Charges," *Proceedings of the 13th JANNAF Combustion Meeting*, 1976.

[13] Gough, P. S., "The Influence of an Impact Representation of Internal Boundaries on the Ballistic Predictions of the Nova Code," *Proceedings of the 14th JANNAF Combustion Meeting*, 1977.

[14] Gough, P. S. and Zwarts, F. J., "Modeling Heterogeneous Two-Phase Reacting Flow," *AIAA Journal*, Vol. 17, Jan. 1979, p. 17.

[15] Horst, A. W., Nelson, C., and May, I. W., "Flame Spreading in Granular Propellant Beds," AIAA Paper 77-856, AIAA 10th Fluid and Plasma Dynamics Conference, 1977.

[16] Betchov, R. and Lorenzen, C., "Phase Relations in Isotropic Turbulence," *Physics of Fluids*, Vol. 17, Aug. 1974, pp. 1503-1508.

[17] Uberoi, M. S. and Freymuth, P., "Turbulent Energy Balance and Spectra of the Axisymmetric Wake," *Physics of Fluids*, Vol. 13, Sept. 1970, pp. 2205-2210.

[18] Marble, F. E., "Dynamics of a Gas Containing Small Particles," *Combustion and Propulsion*, Pergamon Press, N.Y., 1963, p. 175.

[19] Marble, F. E., "Dynamics of Dusty Gases," *Annual Reviews of Fluid Mechanics*, Vol. 2, Annual Reviews, Inc., Palo Alto, Calif., 1970, p. 397.

[20] Kendall, R. M. and Bartlett, E. P., "Nonsimilar Solution of the Multicomponent Laminar Boundary Layer by an Integral Matrix Method," *AIAA Journal*, Vol. 6, June 1968, p. 1089.

[21] Crowe, C. T., "Vapor-Droplet Flow Equations," Lawrence Livermore Laboratory, Rept. UCRL-51877, Aug. 1975.

[22] Klingenberg, G. and Mach, H., "In-Core Measurements of Gas Velocity and of Radial Gas Temperature Distributions," *Proceedings of the Fourth International Symposium on Ballistics*, U.S. Naval Postgraduate School, Monterey, Calif., Nov. 1978.

[23] Faist, M. B. and Muckerman, J. T., "Importance Sampling and Histogrammic Representations of Reactivity Functions and Product Distributions in Monte Carlo Quasiclassical Trajectory Calculations," *Journal of Chemical Physics*, Vol. 69, No. 9, 1978, pp. 4087-4096.

[24] Lighthill, M. J., "On Sound Generated Aerodynamically. I. General Theory and II. Turbulence as a Source of Sound," *Proceedings of the Royal Society, London, 211A*, 1952, pp. 564-591 and *222A*, 1954, pp. 1-32.